ADHESION IN SPHERICAL CONTACTS AND IN ELECTROSTATIC ACTUATION OF A CARBON NANOTUBE

A Thesis Presented

by

Yu-Chiao Wu

to

The Department of Mechanical and Industrial Engineering

in partial fulfillment of the requirements

for the degree of

Master of Science

in

Mechanical Engineering

in the field of

Mechanics and Design

Northeastern University
Boston, Massachusetts

July, 2008

CONTENTS

Part I. Plastic Yield Conditions for Adhesive Contacts

Part II. Actuation of a Carbon-Nanotube-Based Switch

ABSTRACT

The Hertz contact theory can predict the onset of yielding for those contacts in which adhesive effect is negligible. However in microscale contacts, yielding will occur for lower loads than predicted by the Hertz theory. The present study provides yield conditions for the JKR, DMT, and Greenwood-Johnson theories of adhesion. Attention is first focused on the initiation of yield along the symmetrical axis of the contact. The results show the critical loads for the three adhesion theories are close together but different significantly from that predicted by Hertz. Results are also obtained for the onset of yielding away from the symmetrical axis using the Greenwood-Johnson theory of adhesion.

The carbon nanotube is a popular component in nanotechnology. This study focuses on one kind of structure in NEMS, i.e. a nanoswitch which consists of a doubly clamped carbon nanotube and an electrode plane. When a voltage difference is applied between them, an electrostatic distributed force is produced to bend the nanotube down toward the electrode plane. This study also discusses the effect of two slip zones around both the ends which releases a portion of the tensile force inside the nanotube. The numerical results compare three models of doubly clamped nanotubes – a nanotube without stretching, a nanotube with stretching but no slip zones, and a nanotube with stretching and slip zones, to a doubly pinned nanotube and a nanowire.

Part I. Plastic Yield Conditions for Adhesive Contacts

Chapter 1. Introduction

The Hertz theory [1], which analyzes the contact between two nonconforming elastic bodies, has been an essential theory in contact mechanics since it was formulated by Hertz in 1882. The assumptions of Hertz theory are: (1) the surfaces are continuous and non-conforming; (2) the dimensions of the contact area are much smaller than the radii of curvature and than the dimensions of these linear elastic isotropic bodies, so that each body can be modeled as an elastic half-space; (3) the contacting surfaces are frictionless; and (4) no tensile stress exists in the contact area, i.e. the adhesive forces are neglected.

In the Hertz analysis, the axis which is perpendicular to the contacting surfaces and passes through the center of the contact (i.e. the *z*-axis) is a principal stress axis. The maximum value of the shear stress is related to the maximum Hertz pressure and occurs on the *z*-axis. For a value of Poisson's ratio of ν = 0.3, Johnson [1] showed that the maximum shear stress is approximately $0.31p_0$ and occurs at a depth of $0.48a$, where p_0 is the maximum contact pressure ($p_0 = 3P/2\pi a^2$), P is the applied force, and "a" is the contact radius. For arbitrary values of Poisson's ratio the maximum contact pressure for the onset of plastic deformation is given by $p_0 = KH$ where the hardness (H) is related to the yield strength by $H = 2.8Y$ [2], and the hardness coefficient K is related to the Poisson's ratio by $K = 0.454 + 0.41\nu$ [3].

Hertz contact theory has been used extensively in a wide variety of applications such as contacts between railroad wheels and the rail, gears, bearings, and various machine components. However Hertz theory neglects the effect of adhesion, which plays an important role in microscale contacts which occur in microswitches and other MEMS devices. In such applications yielding will initiate at a lower applied force than is predicted when adhesion is neglected.

The JKR theory (Johnson, Kendall, and Roberts, [4]) of adhesion is widely used in contact modeling and in the interpretation of experimental results. In this surface energy based model the effect of adhesion is neglected outside the contact area. The solution was derived from a superposition of the stress fields from the Hertz model and those due to a circular flat punch. The contact radius is found by minimizing the sum of the potential energy of the load, the elastic strain energy, and the surface energy. The DMT theory (Derjaguin, Muller, and Toporov, [5]) sets the profile of the contact model to be the same as in the Hertz theory. Thus the force of adhesion acts only to define an equivalent Hertz load, which is the sum of the applied load and the adhesion force. The latter is independent of the level of loading.

It was shown by Tabor [6] that the DMT theory is relevant for $\mu << 1$ and the JKR theory applies for $\mu >> 1$. The Tabor parameter (μ), which is precisely defined later, is basically the ratio of the elastic deformation to the range of surface forces. Muller, Yushchenko, and Derjaguin [7] evaluated the adhesive force by numerically integrating the stress due to the Lennard-Jones potential. The pull-off force was determined and found to depend upon a single dimensionless parameter similar to the Tabor parameter and varied continuously between the DMT and JKR limits. A more comprehensive treatment of this JKR-DMT transition was given by Greenwood [8].

Maugis [9] obtained an analytical solution for the JKR-DMT transition by assuming a simplified law to relate the adhesive stress to the local separation. In this theory, the adhesive stress is taken equal to the theoretical stress in any region in which the local separation is less than a critical value (h_0); it is set to zero wherever the separation is greater than h_0. The value of h_0 is found by equating the work of adhesion of this simplified law to that of the Lennard-Jones potential.

Greenwood and Johnson [10] provided a simpler alternative to the Maugis theory by defining the adhesive zone differently than did Maugis. This contact model superimposes one tensile Hertz contact and one compressive Hertz contact, leading to a displacement field which is spherical in the contact region. Although the form of the adhesion stress versus separation is not predetermined, the work of adhesion and the maximum value of the adhesive stress can be specified. It is these two parameters which were shown by Barthel [11] to be most important in modeling the adhesive interaction. Most importantly, the simple form of the sub-surface stress field makes this theory an attractive candidate to use in order to determine the onset of yielding.

In an adhesive contact, the critical load and the location of initial yielding are different from what they would be without adhesion. Furthermore these values may depend on which theory is applied. In [12] Kadin, Kligerman and Etsion investigated the onset of plasticity during a jump into contact. Results were obtained in the form of an integral equation which was solved numerically. The present study provides yield conditions for the JKR, DMT, and Greenwood and Johnson models of adhesion using the analytical form of the stress fields. As such the results of this investigation should be useful in predicting the onset of yield in microcontacts in which the effect of adhesion is important.

Chapter 2. Subsurface Stress Fields

The Hertz theory is broadly used to analyze contact between nonconforming elastic solids. It is valid for the contact between two spheres which have radii of curvatures R_1 and R_2, elastic moduli E_1 and E_2, and Poisson's ratios ν_1 and ν_2, respectively. This configuration can be used to define an equivalent system for the contact between a rigid sphere with an effective radius R given by

$$\frac{1}{R} = \frac{1}{R_1} + \frac{1}{R_2} \tag{1}$$

and a flat elastic body with an effective modulus E^*.defined as

$$\frac{1}{E^*} = \frac{1-\nu_1^2}{E_1} + \frac{1-\nu_2^2}{E_2} \tag{2}$$

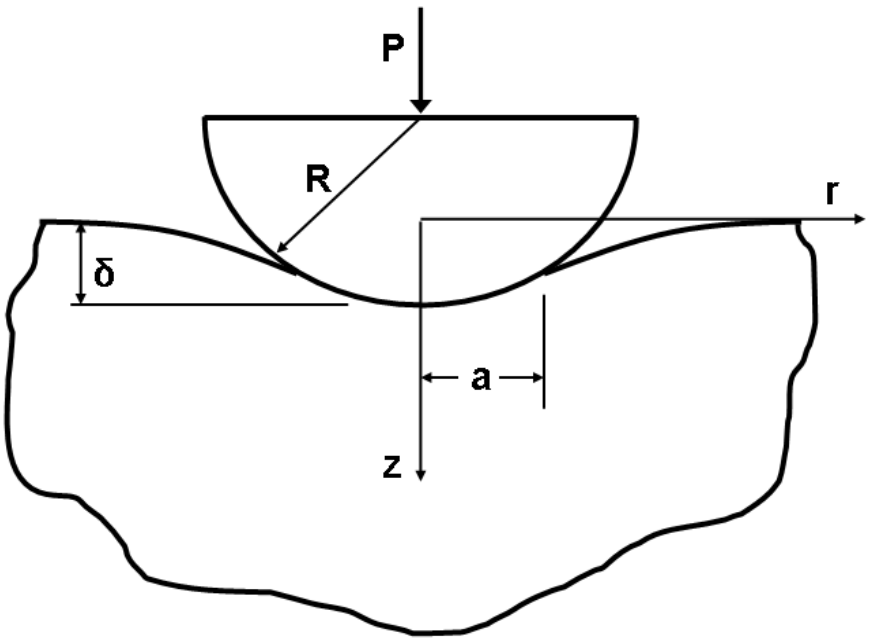

Figure 1. A rigid sphere contacting an elastic half-space.

It is noted that the Hertz theory replaces the spheres by elastic half-spaces. Thus the theory is valid for contacting bodies which are locally spherical provided that the contact dimensions are much smaller than the radii of curvatures.

The surface energy is the energy per unit area needed to form a new surface reversibly and isothermally due to the breaking of bonds and reorganization of atoms near the surface. Unlike molecules in the bulk, molecules near the surface are acted upon by a different set of forces by their neighbors. The work per unit area which is needed to separate two surfaces is

$$w = \gamma_1 + \gamma_2 - \gamma_{12} \tag{3}$$

where γ_1 and γ_2 are the surface energies of the two solids, γ_{12} is the interfacial energy, and w is the Dupré energy of adhesion or the work of adhesion. For the contact of identical bodies the work of adhesion is twice the surface energy. The Tabor parameter μ, described earlier as the ratio of the elastic deformation to the range of surface forces, is an important parameter in describing elastic adhesive contacts and is given by

$$\mu = \left(R w^2 / E^{*2} Z_0^3 \right)^{1/3} \tag{4}$$

where Z_0 is the equilibrium separation distance of the two surfaces.

2.1 Stress field for the JKR model

The stress field of JKR theory [4] is the superposition of the stress field for Hertz and that for a circular flat punch, each with the same contact radius a. In the Hertz model, the normalized stress field is given by [13]:

$$\left(\frac{\sigma_{rr}}{p_m}\right)_H = \frac{1-2\nu}{2(r/a)^2}\left[1-\left(\frac{(z/a)}{\sqrt{t}}\right)^3\right]+\frac{3}{2}\frac{(z/a)}{\sqrt{t}}\left[(1+\nu)\sqrt{t}\tan^{-1}\frac{1}{\sqrt{t}}+(1-\nu)\frac{t}{1+t}+\frac{(z/a)^2}{t^2+(z/a)^2}-2\right],$$

$$\left(\frac{\sigma_{\theta\theta}}{p_m}\right)_H = -\frac{1-2\nu}{2(r/a)^2}\left[1-\left(\frac{(z/a)}{\sqrt{t}}\right)^3\right]+\frac{3}{2}\frac{(z/a)}{\sqrt{t}}\left[(1+\nu)\sqrt{t}\tan^{-1}\frac{1}{\sqrt{t}}-(1-\nu)\frac{t}{1+t}-2\nu\right],$$

$$\left(\frac{\sigma_{zz}}{p_m}\right)_H = -\frac{3}{2s}\left[\frac{(z/a)}{\sqrt{t}}\right]^3, \tag{5}$$

$$\left(\frac{\sigma_{rz}}{p_m}\right)_H = -\frac{3}{2}\frac{(z/a)^2}{\sqrt{t}}\frac{(r/a)}{s(1+t)},$$

$$\left(\frac{\sigma_{r\theta}}{p_m}\right)_H = \left(\frac{\sigma_{\theta z}}{p_m}\right)_H = 0,$$

where

$$s=\left\{\left[(r/a)^2+(z/a)^2-1\right]^2+4(z/a)^2\right\}^{1/2},$$

$$t=\frac{1}{2}\left[(r/a)^2+(z/a)^2-1+s\right],$$

the mean Hertz pressure is $(p_m)_H = \overline{P}_H/\pi a^2$, and $\overline{P}_H$ is the applied compressive load. It is noted that the stress field given in Eqn. (5) corresponds to surface tractions and surface normal displacements given in [1] by

$$\sigma_{zz}(r,0) = -\frac{2E^* a}{\pi R}\sqrt{1-(r/a)^2}, \qquad u_z(r,0)=\frac{1}{2R}(2a^2-r^2), \qquad r\le a \tag{6}$$

For the flat-ended circular punch, the normalized stress field is given in [13] as

$$\left(\frac{\sigma_{rr}}{p_m}\right)_F = -\frac{1}{2}\left\{\frac{(z/a)}{s\sqrt{t}} - \frac{(z/a)}{s^3\sqrt{t}}\left[-s\left(\left(\frac{z}{a}\right)^2 + t\right) + 4\left(\frac{z}{a}\right)^2(1+t)\right] - \frac{(1-2\nu)}{(r/a)^2}\left[1 - \frac{(z/a)}{\sqrt{t}}\right] + \frac{(z/a)\sqrt{t}}{s(1+t)}\right\},$$

$$\left(\frac{\sigma_{\theta\theta}}{p_m}\right)_F = -\frac{1}{2}\left\{2\nu\frac{(z/a)}{s\sqrt{t}} + \frac{(1-2\nu)}{(r/a)^2}\left[1 - \frac{(z/a)}{\sqrt{t}}\right] - \frac{(z/a)\sqrt{t}}{s(1+t)}\right\},$$

$$\left(\frac{\sigma_{zz}}{p_m}\right)_F = -\frac{1}{2}\left\{\frac{(z/a)}{s\sqrt{t}} + \frac{(z/a)}{s^3\sqrt{t}}\left[-s\left(\left(\frac{z}{a}\right)^2 + t\right) + 4\left(\frac{z}{a}\right)^2(1+t)\right]\right\}, \tag{7}$$

$$\left(\frac{\sigma_{rz}}{p_m}\right)_F = -\frac{1}{2}\frac{(r/a)}{s^2}\frac{(z/a)^2}{\sqrt{t}}\left[3 - \frac{4(z/a)^2}{ts}\right]$$

$$\left(\frac{\sigma_{r\theta}}{p_m}\right)_F = \left(\frac{\sigma_{\theta z}}{p_m}\right)_F = 0$$

where the mean flat punch pressure is $(p_m)_F = \overline{P}_F/\pi a^2$, and the tensile rigid punch load is $\overline{P}_F$.

The applied compressive load in the JKR model is given by [4]

$$\overline{P}_{JKR} = \overline{P}_H - \overline{P}_F \tag{8}$$

For a given applied load ($\overline{P}_{JKR}$), the corresponding equivalent Hertz load is given by [4]

$$\overline{P}_H = \overline{P}_{JKR} + 3\pi wR + \sqrt{6\pi wR\overline{P}_{JKR} + (3\pi wR)^2} \tag{9}$$

and the contact radius by

$$a^3 = \frac{3\overline{P}_H R}{4E^*} \tag{10}$$

Finally the corresponding stress field is expressed by

$$\left(\frac{\sigma_{ij}}{p_m}\right)_{JKR}\overline{P}_{JKR} = \overline{P}_H\left(\frac{\sigma_{ij}}{p_m}\right)_H - \overline{P}_F\left(\frac{\sigma_{ij}}{p_m}\right)_F \tag{11}$$

Dimensionless loads are defined by dividing $\overline{P}_{JKR}$ by $3\pi wR$, i.e. $P_{JKR} = \overline{P}_{JKR}/3\pi wR$, and similarly for the Hertz load and flat punch load. Thus Eqn. (9) becomes

$$P_H = P_{JKR} + 1 + \sqrt{2P_{JKR} + 1} \tag{12}$$

Eqn. (8) can be modified to

$$P_F = P_H - P_{JKR} \tag{13}$$

and Eqn. (11) becomes

$$\left(\frac{\sigma_{ij}}{p_m}\right)_{JKR} = \frac{1}{P_{JKR}}\left[P_H\left(\frac{\sigma_{ij}}{p_m}\right)_H - P_F\left(\frac{\sigma_{ij}}{p_m}\right)_F\right] \tag{14}$$

Equation (14) expresses the stress field for the JKR theory in terms of dimensionless quantities. If it is divided by the yield stress (σ_Y) and multiplied by $(p_m)_{JKR}$, it can be written as

$$\left(\frac{\sigma_{ij}}{\sigma_Y}\right)_{JKR} = \frac{3wR}{\sigma_Y a^2}\left[P_H\left(\frac{\sigma_{ij}}{p_m}\right)_H - P_F\left(\frac{\sigma_{ij}}{p_m}\right)_F\right] \tag{15}$$

Now substitute a from Eqn. (8) into Eqn. (15), and use $3wR/\sigma_Y a^2 = \varphi P_H^{-2/3}$ where φ is an adhesion parameter defined by

$$\varphi = \left[\frac{16wE^{*2}}{3\pi^2 R\sigma_Y^3}\right]^{\frac{1}{3}} \tag{16}$$

This adhesion parameter (φ) is the ratio of the maximum contact stress due to a Hertz load equal to $(8/9)\pi wR$ divided by the yield stress.

Thus the stress field for the JKR theory can be written as

$$\left(\frac{\sigma_{ij}}{\sigma_Y}\right)_{JKR} = \varphi P_H^{-2/3}\left[P_H\left(\frac{\sigma_{ij}}{p_m}\right)_H - P_F\left(\frac{\sigma_{ij}}{p_m}\right)_F\right] \tag{17}$$

To summarize, for a given value of the applied load (P_{JKR}), the equivalent Hertz load (P_H) is determined from Eqn. (12), the flat punch load (P_F) is determined by Eqn. (13), and the stress fields are specified by Eqns. (5), (7), and (17), where φ is given by Eqn. (16).

2.2 Stress field for the DMT model

The DMT model is also a well-known theory of adhesive contact which assumes a Hertz profile but with a different load. The relationship between the equivalent Hertz load and the applied load (i.e. the DMT load) is [5]

$$\overline{P}_H = \overline{P}_{DMT} + 2\pi wR \tag{18}$$

or in dimensionless form

$$P_H = P_{DMT} + \frac{2}{3} \tag{19}$$

The stress field in the DMT theory remains the same as the stress field in Hertz theory, i.e.

$$\left(\frac{\sigma_{ij}}{p_m}\right)_{DMT} = \left(\frac{\sigma_{ij}}{p_m}\right)_H \tag{20}$$

and the radius of the contact area (a) is determined by

$$a^3 = \frac{3\left(\overline{P}_{DMT} + 2\pi wR\right)R}{4E^*} \tag{21}$$

At this point, Eqn. (20) can be written as

$$\left(\frac{\sigma_{ij}}{\sigma_Y}\right)_{DMT} = \frac{3}{2}\varphi\left(P_{DMT} + \frac{2}{3}\right)^{\frac{1}{3}}\left(\frac{\sigma_{ij}}{p_m}\right)_H \tag{22}$$

where φ is given by Eqn. (16), and the Hertz stress field is specified by Eqn. (5).

2.3 Stress field for the Greenwood and Johnson model

Greenwood and Johnson [10] presented a theory of adhesive contact which, like the Maugis model, is valid for a broad range of the Tabor parameter. It was developed because the simple form of the surface displacements made it desirable to use in viscoelastic adhesive contacts.

We choose this model for a different reason – the simple form of the subsurface stresses make it an attractive choice for determining the onset of yield.

The Greenwood-Johnson (GJ) model relies on the observation that the superposition of two Hertz contact stress distributions given by

$$\sigma_{zz}(r,0) = -\frac{2E^* a}{\pi R}\sqrt{1-\left(\frac{r}{a}\right)^2}, \quad r < a, \qquad \text{and} \qquad \sigma_{zz}(r,0) = \frac{2E^* c}{\pi R}\sqrt{1-\left(\frac{r}{c}\right)^2}, \quad r < c \tag{23}$$

leads to a uniform rigid body displacement on the surface for $r < a$. Thus the stress field

$$\sigma_{zz}(r,0) = -(1+k)\frac{2E^* a}{\pi R}\sqrt{1-\left(\frac{r}{a}\right)^2} + k\frac{2E^* c}{\pi R}\sqrt{1-\left(\frac{r}{c}\right)^2}, \qquad \text{for} \quad r < a, c \tag{24}$$

where k is an arbitrary constant, leads to the required curvature $(1/R)$ of the deformed surface for $r < a$, and corresponds to adhesive stresses acting in the annular region $a < r < c$. We can now write the subsurface stress field as

$$\sigma_{ij} = (1+k)\frac{2E^* a}{\pi R}\left(\frac{\sigma_{ij}}{p_0}\right)_H - k\frac{2E^* c}{\pi R}\left(\frac{\sigma_{ij}}{p_0}\right)_{H,a\Rightarrow c} \tag{25}$$

where the notation $a \Rightarrow c$ denotes "*a*" being replaced by "*c*". It is noted that for given contact radius (*a*), the values of the outer radius of the adhesion annulus (*c*) and of the parameter *k* have yet to be determined.

These relations will now be written in dimensionless form. Following Greenwood and Johnson [10], we set $a = \beta a^*$, $c = \beta c^*$, and $z = \beta z^*$, where $\beta^3 = R^2 w / E^*$. The load is also made dimensionless by $P_{GJ} = \overline{P}_{GJ} / 3\pi w R$. In [10] an alternative form of the Tabor parameter is provided by $\mu = \sigma_0 \left(R/E^{*2} w\right)^{1/3}$, where $\sigma_0 = w / Z_0$ is approximately the maximum adhesive stress [9]. It is now easy to relate β to μ using

$$\mu = \frac{\sigma_0 R}{E^* \beta} \tag{26}$$

The parameter *m* is defined by $m = c/a$ so that with a^* given, m is determined by [10]

$$\mu a^* \left[a^* \left(m^2 - 1 \right)^{1/2} + \frac{\pi}{2} \mu \right] (m-1)(m+2) = 3(m+1) \tag{27}$$

and the dimensionless applied load is given by

$$P_{GJ} = \frac{2a^{*3}}{3\pi} \left[1 - k\left(m^3 - 1 \right) \right] \tag{28}$$

where the constant, k, is determined from

$$\mu = k \frac{2}{\pi} a^* \left(m^2 - 1 \right)^{\frac{1}{2}} \tag{29}$$

Equation (25) can also be cast in dimensionless form as

$$\left(\frac{\sigma_{ij}}{\sigma_Y} \right)_{GJ} = \varsigma \frac{a^*}{\mu} \left[(1+k) \left(\frac{\sigma_{ij}}{p_0} \right)_H - km \left(\frac{\sigma_{ij}}{p_0} \right)_{H, a \Rightarrow c} \right] \tag{30}$$

where

$$\varsigma = \left(2\sigma_0 / \pi \sigma_Y \right) \tag{31}$$

In summary, for a given a^*, μ, and ς, the parameters *m*, *k* and P_{GJ} are determined from Eqns. (27),(29), and (28) respectively, and the stress field is specified by Eqn. (30).

Chapter 3. Results and Discussion

Plastic yielding of ductile materials can be predicted using the von Mises yield criterion, which corresponds to the second invariant of the deviatoric stress tensor (or equivalently to the maximum distortional strain energy) reaching a critical value. The von Mises stress is defined as

$$\sigma_{VM} = \frac{1}{\sqrt{2}}\sqrt{\left(\sigma_{rr}-\sigma_{\theta\theta}\right)^2+\left(\sigma_{\theta\theta}-\sigma_{zz}\right)^2+\left(\sigma_{rr}-\sigma_{zz}\right)^2+6\left(\sigma_{r\theta}^2+\sigma_{\theta z}^2+\sigma_{rz}^2\right)} \tag{32}$$

so that yielding occurs when $\sigma_{VM} = \sigma_Y$. It is noted that in axisymmetric problems, the *z*-axis is a principal stress axis so that σ_{rr}, $\sigma_{\theta\theta}$, and σ_{zz} along the *z*-axis are principal stresses. Furthermore $\sigma_{rr} = \sigma_{\theta\theta}$ so that on the *z*-axis Eqn. (32) becomes

$$\sigma_{VM} = \left|\sigma_{rr}-\sigma_{zz}\right| \tag{33}$$

and in this case the von Mises yield condition is equivalent to the Tresca (maximum shear stress) criterion. In the three models considered a sphere indents an elastic half-space as shown in Figure 1. The applied load *P* can represent P_{JKR}, P_{DMT}, or P_{GJ} depending on the model chosen.

3.1 Subsurface von Mises stress fields

The subsurface von Mises stress field contours for the JKR model on the verge of yielding are plotted using Eqns. (17) and (32) for $\varphi = 0.600$ and $P_{JKR} = 4.90$ in Figure 2.

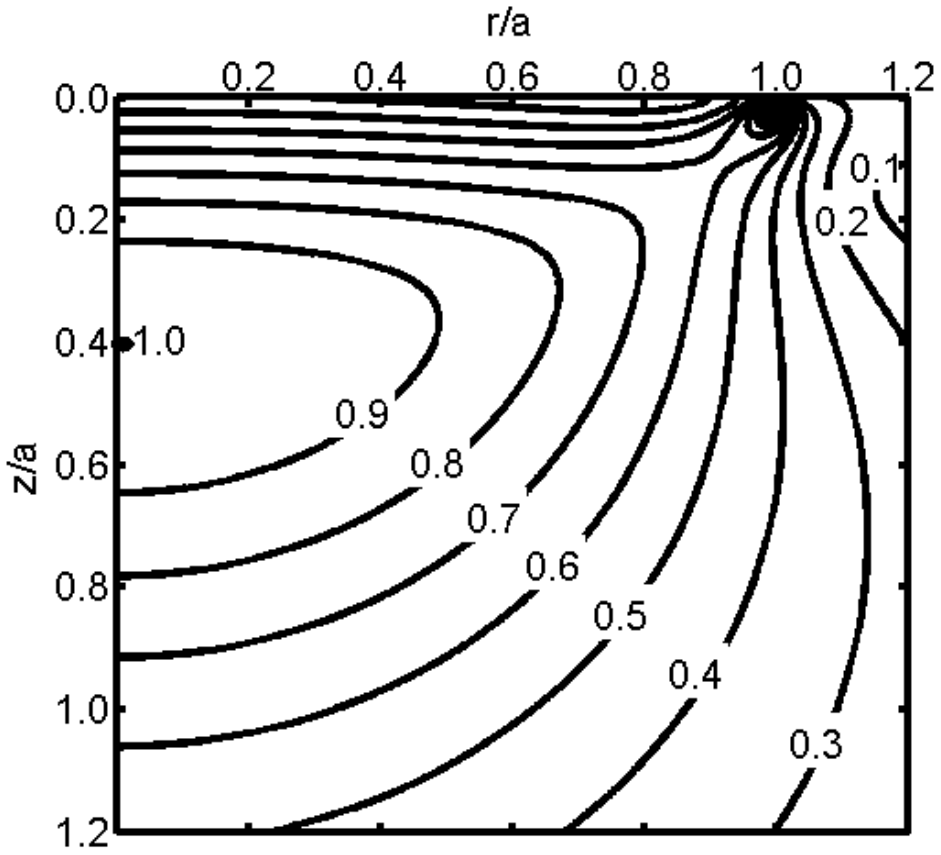

Figure 2. Subsurface von Mises stress contours for the JKR theory with $\nu = 0.3$, $\varphi = 0.600$ and $P_{JKR} = 4.90$ which corresponds to the onset of yield at z/a = 0. 409.

It is noted that the stress field is singular at the boundary of the contact region as is also true at the tip of a crack. Thus we only considered yield on the *z*-axis when using JKR theory. Similarly the subsurface von Mises stress field for the DMT theory is plotted using Eqns. (22) and (32) for $\varphi = 0.600$ and $P_{DMT} = 5.09$ in Figure 3.

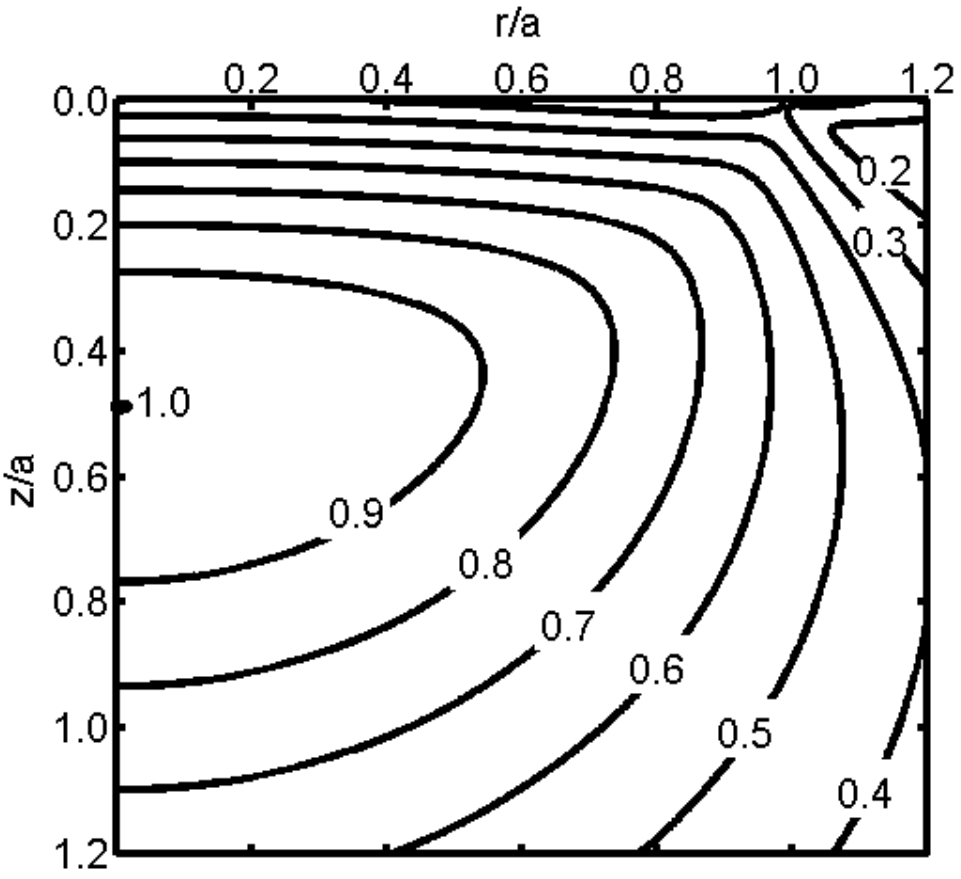

Figure 3. Subsurface von Mises stress contours for the DMT theory with $\nu = 0.3$, $\varphi = 0.600$ and $P_{DMT} = 5.09$ which corresponds to the onset of yield at z/a = 0.481.

Note that from the discussion in the previous section, the stress field is identical to the Hertz stress field. Finally the subsurface von Mises stress field contours at the verge of yielding using Eqns. (30) and (32) for $\varphi = 0.600$ are shown in Figures 4 and 5 for $\mu = 1$ and $P_{GJ} = 4.91$, and for $\mu = 2$ and $P_{GJ} = 4.90$ respectively.

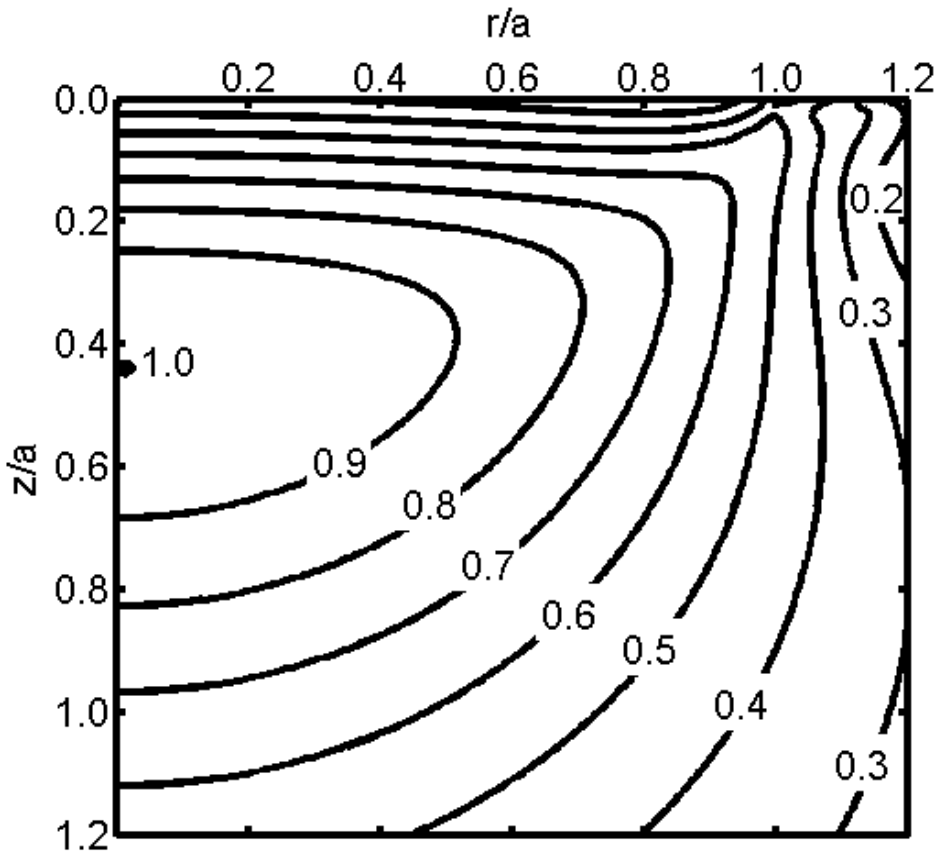

Figure 4. Subsurface von Mises stress contour for the GJ theory with $\nu = 0.3$, $\mu = 1$, $\varphi = 0.600$ and $P_{GJ} = 4.91$, which corresponds to the onset of yield at z/a = 0.434.

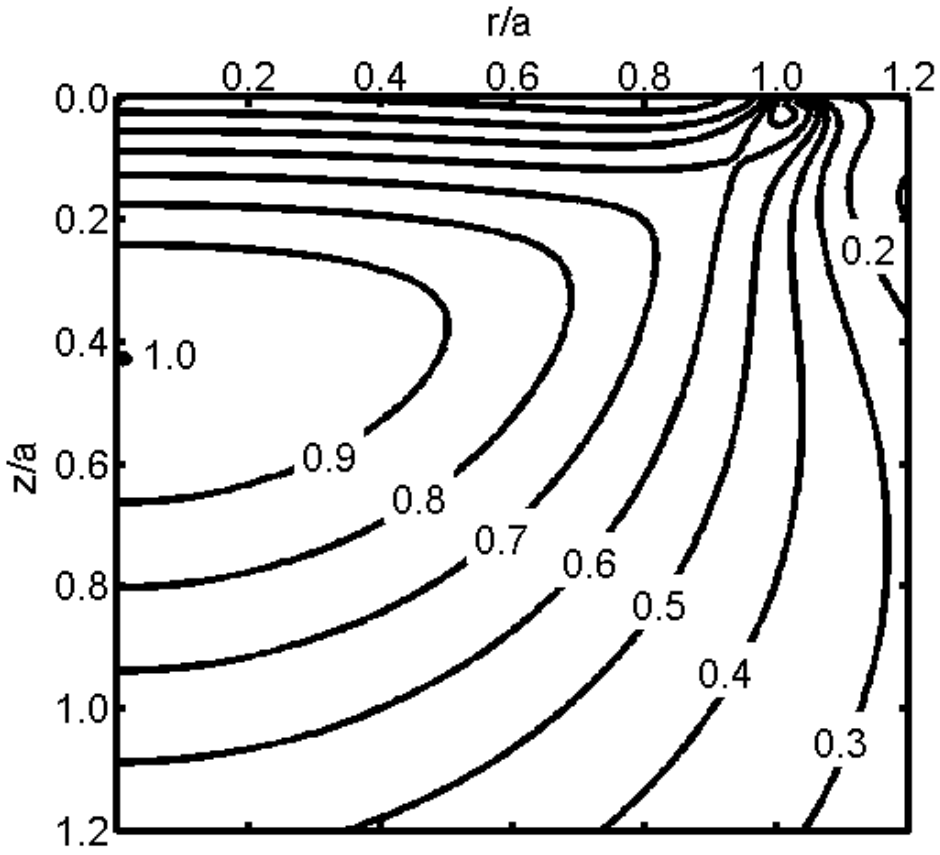

Figure 5. Subsurface von Mises stress contour for the GJ theory with $\nu = 0.3$, $\mu = 2$, $\varphi = 0.600$ and $P_{GJ} = 4.90$, which corresponds to the onset of yield at z/a = 0.423.

In order to determine the onset of yield, we must determine the maximum von Mises stress for each of the adhesion theories from Eqn. (32). In the JKR theory for a given applied load (P_{JKR}), we calculate Φ_{JKR} according to

$$\Phi_{JKR}(P_{JKR}) = \left[\varphi^{-1}\left(\frac{\sigma_{VM}}{\sigma_Y} \right)_{JKR} \right]_{MAX} \tag{34}$$

which depends only on Poisson's ratio and the applied load and is independent of φ. Then the corresponding value of φ to cause yield is

$$\varphi = \Phi_{JKR}^{-1} \tag{35}$$

The outset of yielding in the DMT model depends on the stress term of Eqn. (22), i.e. the Hertz stress. Hence yield always occurs along the z-axis. The maximum value of the von Mises stress field is

$$\Phi_{DMT}(P_{DMT}) = \left[\varphi^{-1}\left(\frac{\sigma_{VM}}{\sigma_Y} \right) \right]_{DMT}^{MAX} \tag{36}$$

which depends only on Poisson's ratio and the applied force, and is independent of ϕ. Then for given P_{DMT}, the value of φ which causes yield is

$$\varphi = \left(\Phi_{DMT} \right)^{-1} \tag{37}$$

In the GJ model, the stress term of Eqn. (30) depends not only on the applied force (or equivalently the contact radius) but also on the Tabor parameter (μ). The maximum value of the von Mises stress field is

$$\Phi_{GJ}(\mu, a^*) = \left[\varsigma^{-1}\left(\frac{\sigma_{VM}}{\sigma_Y} \right) \right]_{GJ}^{MAX} \tag{38}$$

which depends only on Poisson's ratio, the Tabor parameter, and the contact radius, but is independent of ς. Then for given a^* and μ, the value of ς which causes yield is

$$\varsigma = \left(\Phi_{GJ} \right)^{-1} \tag{39}$$

From Eqns. (4), (16), and (31), the coefficients φ, μ, and ς are related by

$$\varphi = \left(\frac{2\pi}{3} \right)^{\frac{1}{3}} \frac{\varsigma}{\mu} \tag{40}$$

If we now make write for the GJ model

$$\varphi^3 P_{GJ} = \frac{16E^2 \overline{P}_{GJ}}{9\pi^3 R^2 \sigma_Y^3} \tag{41}$$

the quantity $\varphi^3 P_{GJ}$ is the dimensionless force at which yield is initiated. Similarly equations such as Eqn. (41) may be written for $\varphi^3 P_{JKR}$ and $\varphi^3 P_{DMT}$, for the JKR and DMT models respectively.

Results are given for $\varphi^3 P_{JKR}$, $\varphi^3 P_{DMT}$, and $\varphi^3 P_{GJ}$ (for $\mu = 1$ and $\mu = 2$) vs. the adhesion parameter (φ) in Figure 6, which corresponds to yield on the *z*-axis, for three different values of Poisson's ratio. The results for the three theories are very close together. It is only for a Poisson's ratio of one-half and large values of the adhesion parameter that the difference is significant. For small values of the adhesion parameter, all three theories show that the onset of yield approaches that predicted by Hertz contact theory. However as the adhesion parameter increases the force required to initiate yielding decreases and, in fact, becomes zero for sufficiently large values of φ.

The results for the GJ theory are very close to the JKR model. Curve-fit expressions were obtained for the GJ model (for $\mu = 1$ and $\mu = 2$) and are given by

$$\varphi^3 P = 0.0956\varphi^4 - 0.7563\varphi^3 - 0.0472\varphi^2 + 0.0050\varphi + 0.8034, \quad \text{for } \nu = 0.1$$

$$\varphi^3 P = 0.1110\varphi^4 - 0.8236\varphi^3 - 0.0636\varphi^2 + 0.0087\varphi + 1.2429, \quad \text{for } \nu = 0.3 \tag{42}$$

$$\varphi^3 P = 0.1378\varphi^4 - 0.9441\varphi^3 - 0.0579\varphi^2 + 0.0092\varphi + 1.9600, \quad \text{for } \nu = 0.5$$

where these curves had an average error of less than 1% with the GJ model for $\mu = 1$ and $\mu = 2$.

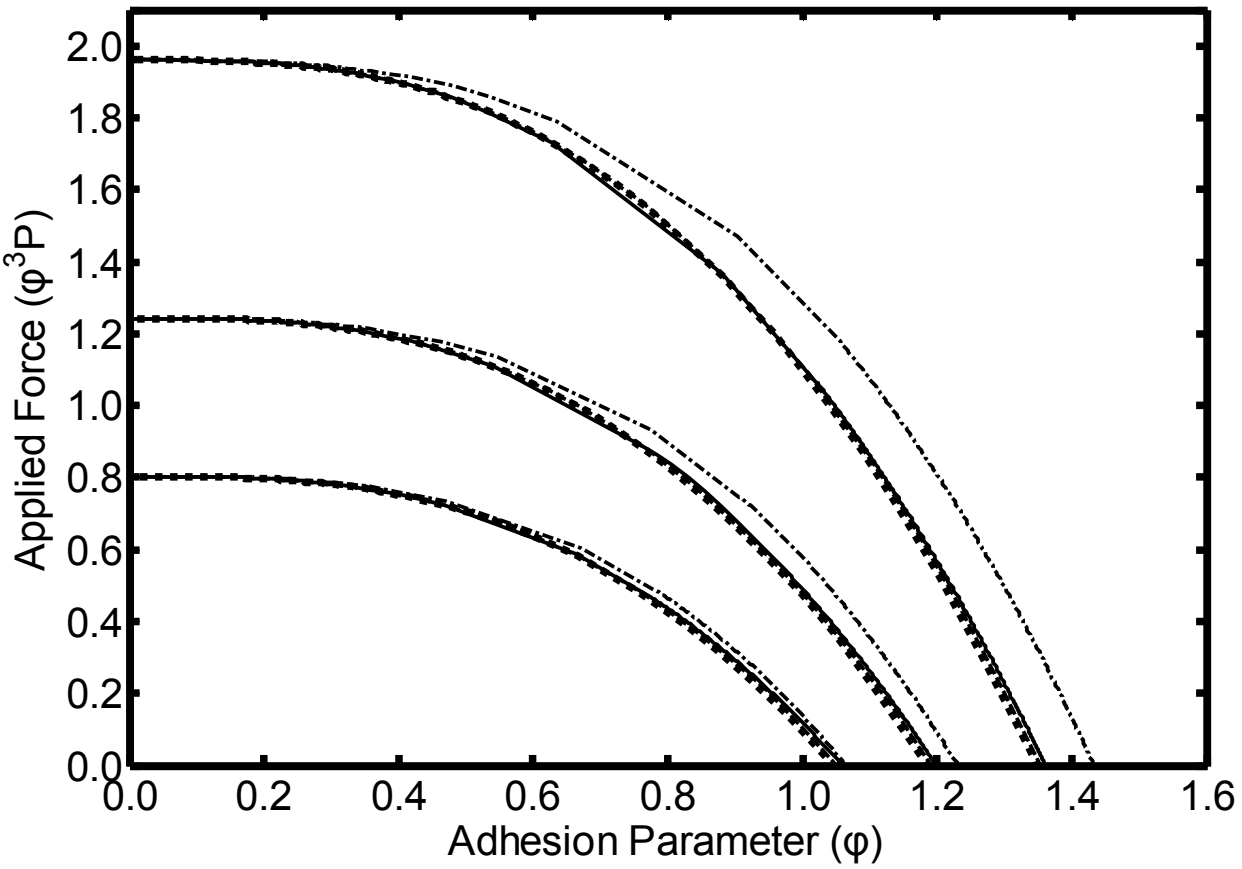

Figure 6. Dimensionless load for the initiation of yield vs. the adhesion parameter for different values of Poisson's ratio. Results are for JKR theory ($\varphi^3 P_{JKR}$ in solid lines), DMT theory ($\varphi^3 P_{DMT}$ in dot-dashed lines), and GJ theory ($\varphi^3 P_{GJ}$ with $\mu = 1$ in dotted lines and with $\mu = 2$ in dashed lines).

It is noted that yield away from the *z*-axis will always occur with the JKR model because of the artificial stress singularity at the edge of the contact. On the other hand in the DMT the stress distribution is the same as in the Hertz theory (but with a higher load) and so yielding always initiates on the *z*-axis. For those reasons neither the JKR or DMT theories are applicable to predict the onset of yield away from the *z*-axis. The possibility of the onset of yield away from the *z*-axis was investigated using the GJ theory for various values of μ as shown in Figure 7 for

$\nu = 0.3$. As can be observed in Figure 7, yielding initiates on the z-axis for sufficiently small values of the adhesion parameter. The transition value of the adhesion parameter (φ) decreases as the Tabor parameter increases.

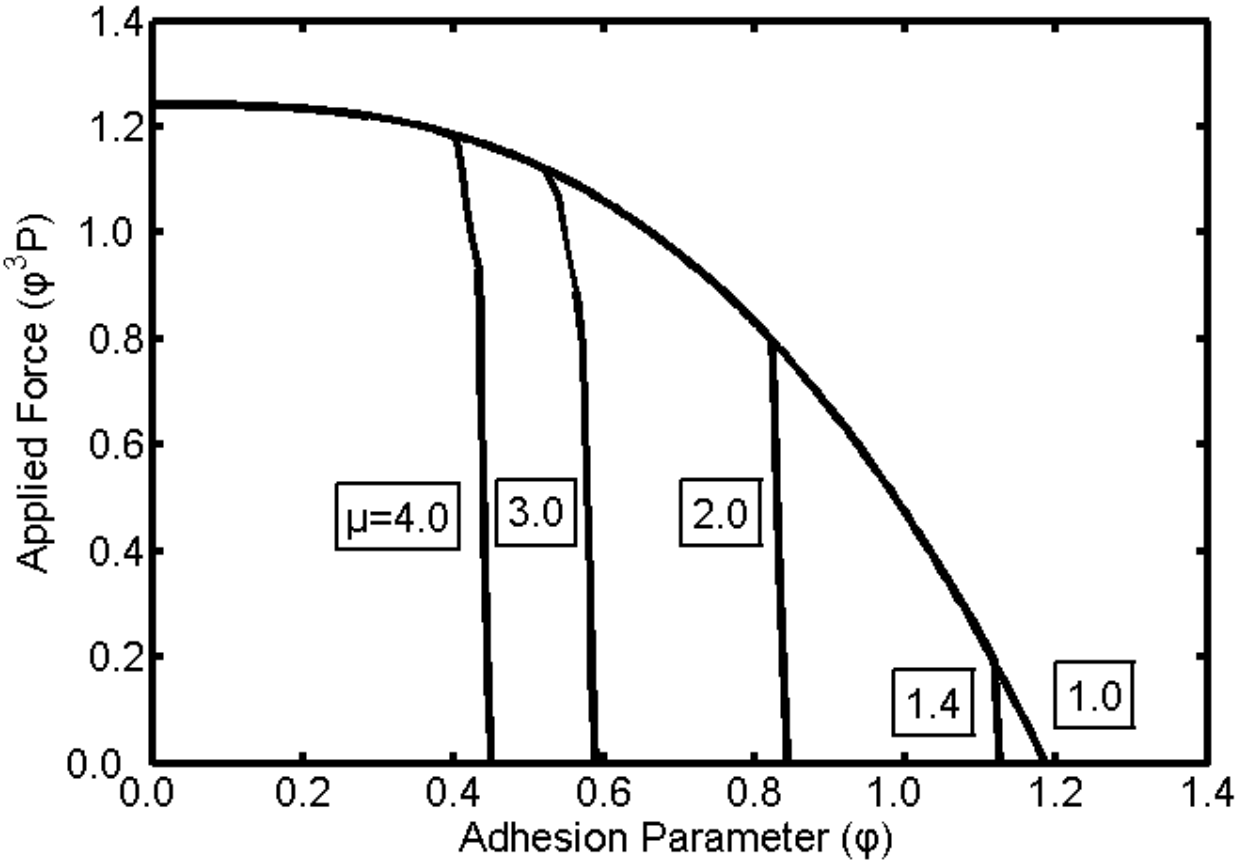

Figure 7. Dimensionless load for the initiation of yield vs. the adhesion parameter for GJ theory ($\mu = 1$, 1.4, 2.0, 3.0, and 4.0) and for a Poisson's ratio of 0.3. Results include yield away from the axis of symmetry which are shown in the nearly vertical lines.

Chapter 4. Conclusions

In microscale contacts, the effect of adhesion is to cause the load required to initiate plastic deformation to be far less than predicted by Hertz contact. This paper has reported results for the onset of yield using three different theories (JKR, DMT, and GJ) of adhesion. The results for all three adhesion models are similar and show that the onset of yield depends primarily on an adhesion parameter φ defined here. Curve-fit formulae are given for the yield load as a function of the adhesion parameter. For a sufficiently large value of the adhesion parameter, yield can occur without the presence of an external load.

Part II. Actuation of a Carbon-Nanotube-Based Switch

Chapter 5. Introduction

Carbon nanotubes (CNTs) are widely applied in Nanoelectromechanical systems (NEMS) due to their ideal electronic and mechanical properties. CNTs' perfect molecular structure, small size, and low density enable the devices to achieve the nanoscale, and their extremely high elastic stiffness and strength [14] make them an excellent mechanical component in NEMS. Some applications of NEMS based on CNTs have been reported, such as nanotweezers [15], random access memory devices [16], nanorelays [17], and rotational actuators [18]. This study discusses a special application of CNTs — a nanoswitch, which is one essential structure in NEMS devices, e.g. random access memories, high-frequency-operated device, and fast switching in communication network. Nanoswitches are usually built by CNTs as combinations of a cantilever beam or a doubly clamped beam and a plane electrode [19]. The doubly clamped case is shown in Fig. 8. When the nanotube charges, the difference of voltage between the

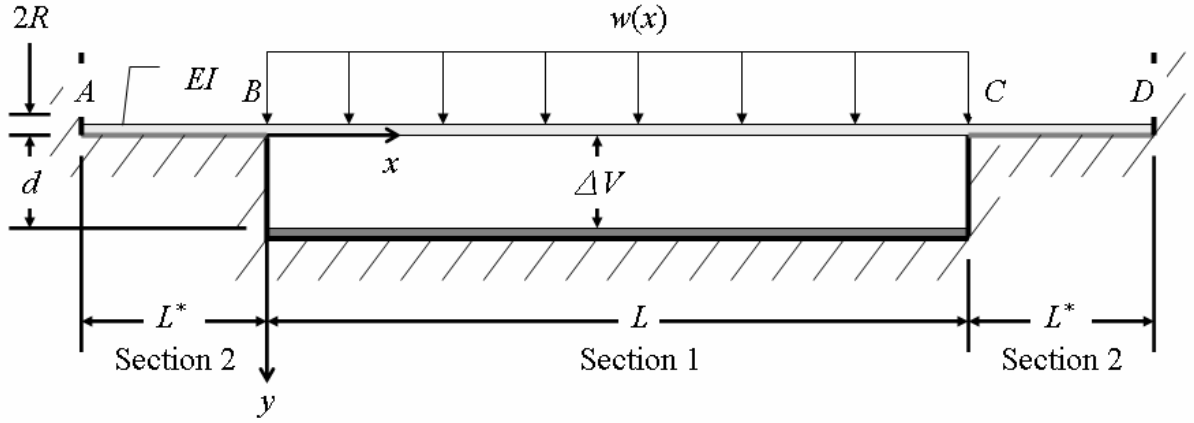

Figure 8. Structure of the carbon-nanotube-based nanoswitch.

nanotube and the electrode produces an electrostatic force to bend the nanotube downward. Then the nanotube becomes close to the electrode gradually with the voltage increasing. However, there is a maximum voltage to keep the nanotube under equilibrium. If the voltage exceeds the maximum voltage, the nanotube will snap down directly to the electrode. The phenomenon is called snapthrough [20].

In the nanoscale, the molecular dynamics (MD) is a common approach for simulation. However, there are usually more than one million atoms involved in a system. Therefore, MD simulation takes much time to compute all atoms of a system and can not be easily used for design optimization. The continuum mechanics was verified to be an appropriate approach of CNTs. Dequesnes *et al* [19] compared the analysis of beam theory to the experimental data [21] for a cantilever nanotube and obtained a good match for both the results. Thus, the mechanical behavior of CNTs can be analyzed easily by using beam theories.

Due to the small scale, the effect of van der Waals force becomes significant, which is an interaction between atoms and derived by using the Lennard-Jones Potential [13] which has an attractive part and a repulsive part. Dequesnes *et al* [19, 22] compared the results including to excluding the effect of van der Waals force. In the viewpoint of scale, the effect of van der Waals is obvious for a long nanotube with a small gap between the tube and electrode. In the viewpoint of structure, van der Waals force affects the deflection of a cantilever nanotube more obviously than a doubly clamped nanotube.

The stretching is a significant role for a doubly clamped nanotube. Due to both ends fixed, the length after deformation is longer than the original length or the distance between two fixed ends. Thus, an axial elongation will be produced. Dequesnes *et al* [22] and Ke *et al* [23] provided the results with stretching for different scales. A nanotube with stretching becomes stiffer than

one without the stretching. In other words, a nanotube with stretching is needed larger voltage for bending. However, for nanotubes with same length, the difference between the case with stretching and without stretching decreases with the gap between the nanotube and the electrode decreasing.

The distribution of charges on the nanotube is an interesting issue for this nanoswitch. Ke *et al* [24] investigated a finite-length conductive nanoscale cylinder and obtained that charges concentrate on both ends and distribute uniformly along its central part. However, the concentration of charges on both ends is negligible. The reason is that both ends are fixed and which deflections are not affected by the concentration of charges.

This study keeps discussing the importance of stretching of a conductive nanotube. Furthermore, two slip zones will be added inside both the ends (Section 2 in Fig. 8) in order to release the internal axial tensile force. The small deformation theory is chosen to analyze all the cases. Then the assumptions are the radius R of the cross-section area of the nanotube and the depth of the trench d much smaller than the width of the electrode and the length of the nanotube L. The slope of the flexural deformation dy/dx can be considered very small, and then the curvature approximates to the second derivative of the deflection d^2y/dx^2. In this study, the Bernoulli – Euler theory is applied to analyze the beam-like behavior of the nanotube, which assumption is to neglect the shear deformations compared to bending deflection. Therefore, the cross-section area of the nanotube remains perpendicular to the neutral axis of the nanotube after deformation.

Chapter 6. External Distributed Forces

6.1 Electrostatic distributed force

As introduced in the chapter 5, a nanotube consisting of a conductive nanotube and a plane electrode is discussed in this study. Due to the effect of charge concentration on the both ends neglected, this system can be considered as a combination of an infinitely long conductive wire with a radius R of the cross-section area and a conductive plane with infinite length and width. The capacitance per unit length for this combination is given by [19]:

$$C = \frac{\pi\varepsilon_0}{\ln\left[1+\frac{r}{R}+\sqrt{\left(\frac{r}{R}+1\right)^2-1}\right]} \tag{43}$$

where r represents the distance from the bottom of the wire to the top of the electrode, that is $r = d - y$ and ε_0 is the permittivity of vacuum or air and $\varepsilon_0 = 8.84\times10^{-12}$ (F/m). The electrostatic energy restored in this type of capacitance is given by [25]:

$$W_e = \frac{1}{2}CV^2 \tag{44}$$

where V is the electric potential between the wire and the plane. Substitute Eqn. (44) into Eqn. (43), the electrostatic energy per length is written as:

$$W_e = \frac{\pi\varepsilon_0 V^2}{2\ln\left[1+\frac{r}{R}+\sqrt{\left(\frac{r}{R}+1\right)^2-1}\right]} \tag{45}$$

The electrostatic distributed load for this case is produced by the gradient of the electrostatic energy per unit length, that is

$$\vec{w}_e = -\nabla W_e \tag{46}$$

Substitute Eqn. (45) into Eqn. (46), the electrostatic distributed load is obtained:

$$w_e = \frac{\pi \varepsilon_0 V^2}{R\sqrt{\frac{r(r+2R)}{R^2}}\left\{\ln\left[1+\frac{r}{R}+\sqrt{\frac{r(r+2R)}{R^2}}\right]\right\}^2} \tag{47}$$

where $r = d - y$.

6.2 van der Waals distributed force

Dequesnes *et al* [19] derived the attractive van der Waals forces per unit length between a carbon nanotube and a graphite ground plane, which is given by:

$$w_{vdW} = \frac{C_6 \sigma^2 \pi^2 R\sqrt{r(r+2R)}(8r^4 + 32r^3R + 72r^2R^2 + 80rR^3 + 35R^4)}{2r^5(r+2R)^5} \tag{48}$$

where $C_6 = 15.2eV\,\mathrm{A}^{\circ 6}$ [26] represents a constant which characterizes the interactions between the two carbon atoms, $\sigma \cong 38nm^{-2}$ means the graphite surface density, and $r = d - y$. The repulsed part of van der Waals force is negligible due to its value much smaller than the attractive van der Waals force's.

In the real model of a nanoswitch, the plane electrode is made of gold, not a graphene sheet. Therefore, Eqn. (48) is not appropriately used for application of this nanoswitch. Thus, the exact equation for a carbon nanotube and an gold electrode plane shall be derived in future investigation.

Chapter 7. Doubly Clamped Nanotube

7.1 Governing equation for a doubly clamped nanotube

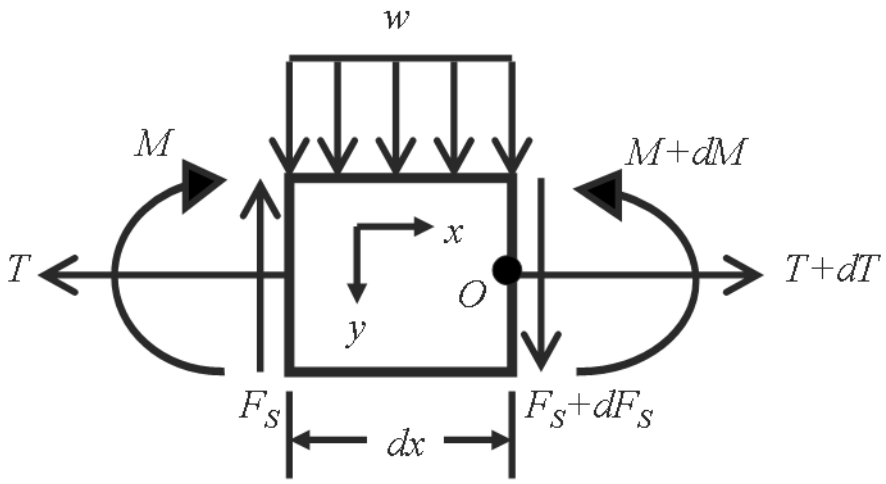

Figure 9. Free-body diagram of segment *dx* at Section 1 of nanoswitch.

To obtain the governing equation for a doubly clamped nanotube, an infinitesimal element with length of *dx* on the nanotube is used to analyze the equilibrium of forces. Its free-body diagram is shown in Fig. 9. The equilibrium equation of forces along the y-direction is given by:

$$+\downarrow \sum F_y = 0: \quad -F_S + \left(F_S + \frac{dF_S}{dx}dx\right) - T\frac{dy}{dx} + \left[T\frac{dy}{dx} + \frac{d}{dx}\left(T\frac{dy}{dx}\right)dx\right] + \left[w_e(x) + w_{vdW}(x)\right]dx = 0$$

$$\frac{dF_S}{dx} + T\frac{d^2y}{dx^2} = -\left[w_e(x) + w_{vdW}(x)\right] \tag{49}$$

where T represents the internal tensile force of the beam, and it will be derived in the next discussion, and $w_e(x)$ and $w_{vdW}(x)$ are the electrostatic force given by Eqn. (47), and van der Waals force given by Eqn. (48), respectively. The equation of equilibrium of the moments at

Point *O* is given by:

$$\sum M_o = 0: \qquad -F_S dx - M + \left[w_e(x) + w_{vdW}(x)\right]dx(kdx) + (M + dM) = 0$$

where k is a proportional constant of distance and $0 < k < 1$ [27]. Due to $dx \to 0$, then the term of external distributed loads is negligible. Then the equilibrium equation of moments becomes:

$$F_S = \frac{dM}{dx}$$

where the bending moment corresponding to the 2nd derivative of the deflection is given by:

$$M = -EI\frac{d^2y}{dx^2}$$

where E is the Young's modulus, and I is the second-area moments, that is $I = \pi(r_{ext}{}^4 - r_{int}{}^4)/4$. Substitute the moment M into the shear force F_S , and then

$$F_S(x) = \frac{d}{dx}\left(-EI\frac{d^2y}{dx^2}\right) = -EI\frac{d^3y}{dx^3}$$

Substitute F_S into Eqn. (49), the governing equation for this beam can be established:

$$EI\frac{d^4y}{dx^4} - T\frac{d^2y}{dx^2} = w_e(x) + w_{vdW}(x) \tag{50}$$

where T means the internal tensile force of the beam, and $w_e(x)$ and $w_{vdW}(x)$ are the electrostatic force given by Eqn. (47), and van der Waals force given by Eqn. (48), respectively. The boundary conditions are given by:

$$y(0) = 0, \quad y'(0) = 0, \quad y(L) = 0, \quad y'(L) = 0$$

7.2 Effect of axial force due to stretching

7.2.1 Stretching in the slip zone

Now the nanotube is considered to be stuck on the ground in Section 2 of Fig. 8.

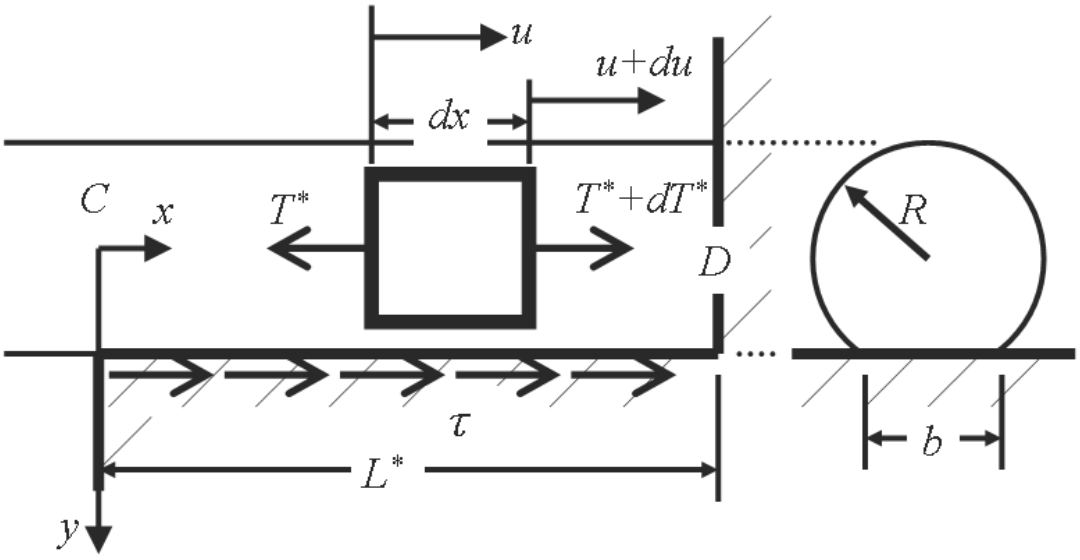

Figure 10. Free-body diagram of segment *dx* at slip zone.

When the nanotube begins bending, a tensile force due to stretching exerts on Point C of Fig. 10. This tensile force elongates the nanotube between Point C and D. However, the shear stress τ exists between the sticking surfaces in order to reduce the internal tensile force, and the tensile force vanishes at Point D. That also means no displacement at Point D for the nanotube. Thus, Section 2 is called "slip zone".

For the dimensions of the slip zone, the length and width are L^* and b respectively. From free-body diagram of segment *dx* shown in Fig. 10, the equilibrium equation of internal tensile forces along the x-direction in the contact region is given by:

$$+\rightarrow \sum F_x = 0: \qquad -T^* + T^* + dT^* + \tau b dx = 0$$

$$\frac{dT^*}{dx} = -\tau b \tag{51}$$

The axial displacement u of the beam dependent on the internal tensile force is written as:

$$du = \frac{T^* dx}{EA}$$

Then
$$T^* = EA\frac{du}{dx} \tag{52}$$

Substitute Eqn. (52) into Eqn.(51), and then

$$EA\frac{d^2u}{dx^2} = -\tau b \tag{53}$$

In the slip zone, the nanotube has no elongation and no internal tensile force at Point *D*. In the opposite, the internal tensile force at Point *C* reaches the value *T* in the deflecting portion of the nanotube. Thus the boundary conditions are given by:

$$EAu'(0) = T\,,\quad EAu'(L^*) = 0\,,\quad u(L^*) = 0$$

Then the general solution of Eqn. (53) is written as:

$$u = -\frac{\tau b}{2EA}x^2 + c_1 x + c_2 \tag{54}$$

where c_1 and c_2 are constants. Substitute the boundary conditions into Eqn. (54), L^*, c_1, and c_2 are obtained:

$$\begin{aligned} L^* &= \frac{T}{\tau b} \\ c_1 &= \frac{T}{EA} \\ c_2 &= -\frac{T^2}{2EA\,\tau b} \end{aligned} \tag{55}$$

Thus, the displacement in the slip zone of the beam is established:

$$u = -\frac{\tau b}{2EA}x^2 + \frac{T}{EA}x - \frac{T^2}{2EA\,\tau b} \tag{56}$$

7.2.2 Stretching in the beam

To obtain the internal tensile force of the beam can be solved by the following two steps.

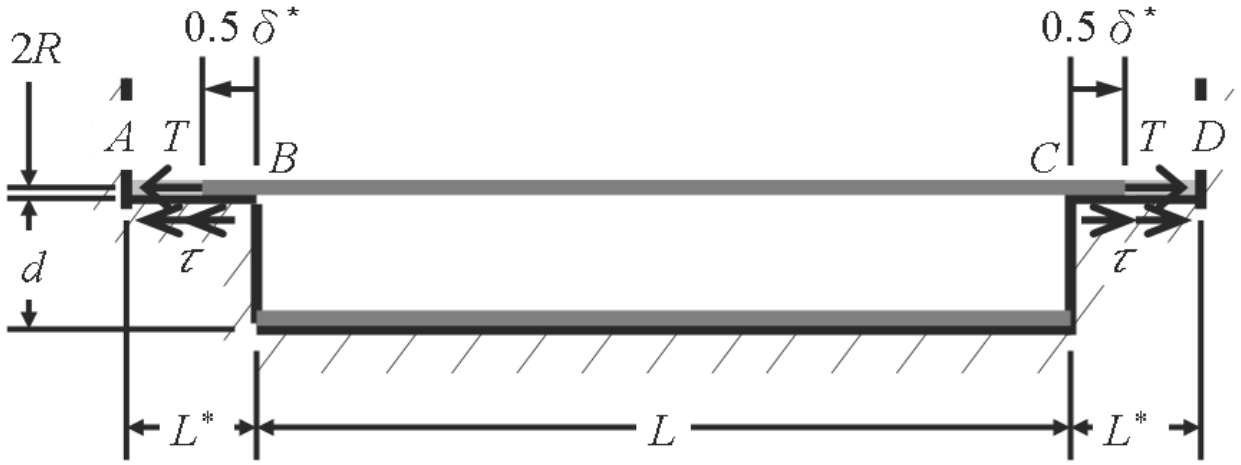

Figure 11. Schematic of the nanotube stretched by tensile forces T.

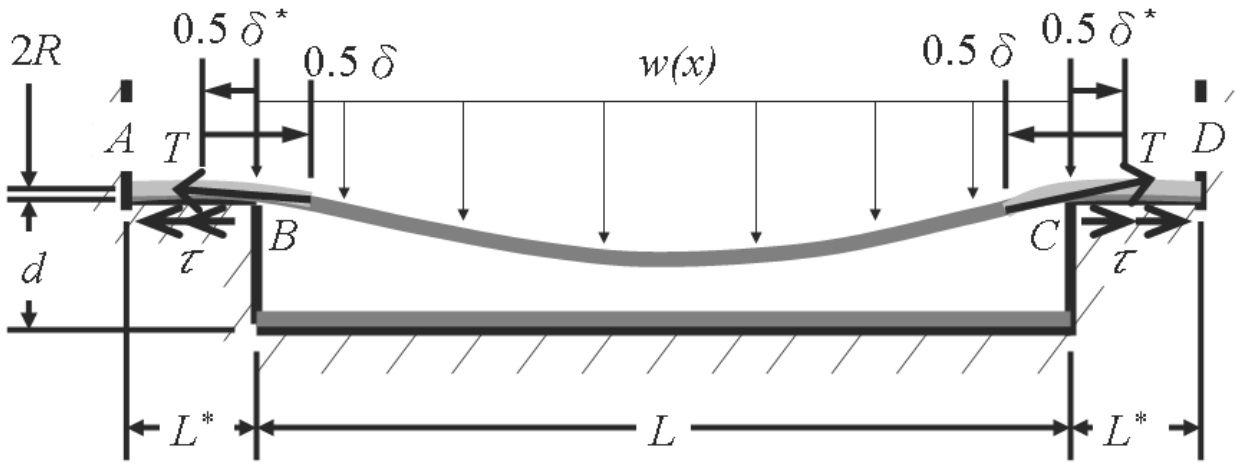

Figure 12. Schematic of the nanotube stretched by external distributed loads $w(x)$.

First, the beam is elongated by the tensile force T along the axial direction shown in Fig. 11. Then, the displacement δ^* due to the internal tensile force can be written as:

$$\delta^* = \frac{L}{EA}T \tag{57}$$

Second, the external forces (including the electrostatic forces and van der Waals forces) apply

upon the nanotube shown in Fig. 12. The displacements δ due to the external forces will move back and is written as:

$$\delta = \int_0^L (ds - dx) = \int_0^L \left(\frac{ds}{dx} - 1 \right) dx = \int_0^L \left(\frac{\sqrt{dy^2 + dx^2}}{dx} - 1 \right) dx \approx \frac{1}{2} \int_0^L \left(\frac{dy}{dx} \right)^2 dx \tag{58}$$

The difference between δ^* and δ equals the displacements on both the boundaries of the slip zones, $u(0)$. Thus

$$\delta^* - \delta = 2u(0) \tag{59}$$

Recall $u(0) = -T^2 / 2EA\tau b$. Thus, Eqn. (59) can be written as:

$$\frac{1}{EA\tau b} T^2 + \frac{L}{EA} T - \frac{1}{2} \int_0^L \left(\frac{dy}{dx} \right)^2 dx = 0 \tag{60}$$

The internal tensile force of the nanotube can be obtained by solving the above quadratic equation.

In the limit case: $\tau \to \infty$, which means that the ends of the nanotube are clamped, and the slip zones disappear. Equation (60) becomes:

$$T = \frac{EA}{2L} \int_0^L \left(\frac{dy}{dx} \right)^2 dx \tag{61}$$

This mechanism of the nanotube can be considered as an equivalent system shown in Fig. 13 [28]. When the nanotube starts bending, the elongation of an effective spring equals the slip distance at the boundary of the nanotube,

$$\delta_S = u(0) = -\frac{T}{k_{eff}} \tag{62}$$

Thus, the effective stiffness coefficient k_{eff} is written as:

$$k_{eff} = \frac{2EA\tau b}{T} \tag{63}$$

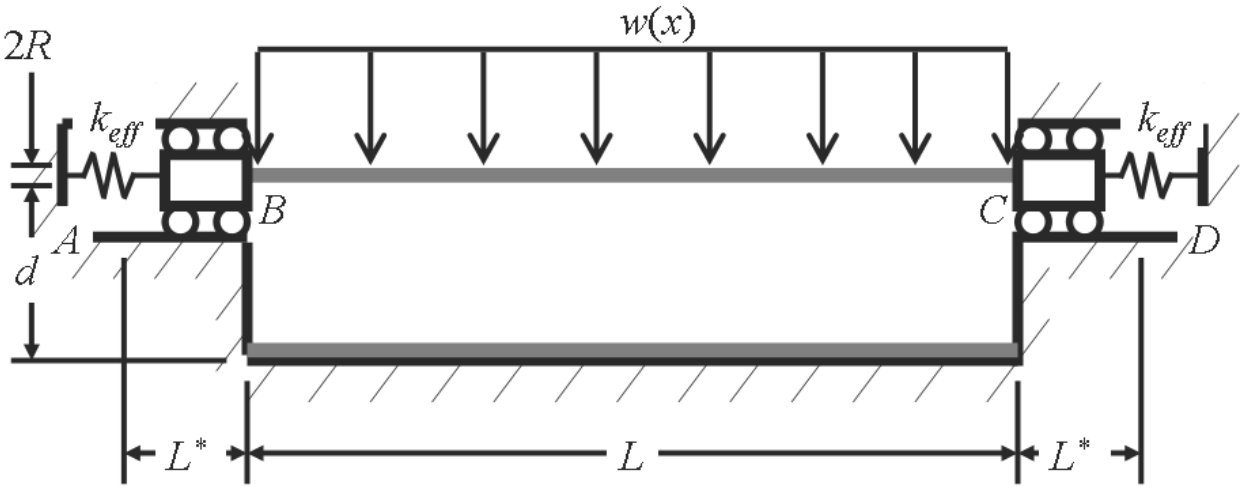

Figure 13. Equivalent model of a nanotube with slip zones.

When $k_{eff} \to \infty$, that is, τ is very large, or T is very small, the nanotube is same as a fixed-fixed beam. This situation can also be proved in Eqn. (60). The first term obtained by the slip zone of Eqn. (60) will vanish if τ is very large or T is very small. Because dy/dx in the third term of Eqn. (60) depends on the voltage, the tension T also depends on the voltage V. Therefore, the effective stiffness coefficient k_{eff} varies with the voltage contrary.

Chapter 8. Doubly Pinned Nanotube and Nanowire

8.1 Doubly pinned nanotube

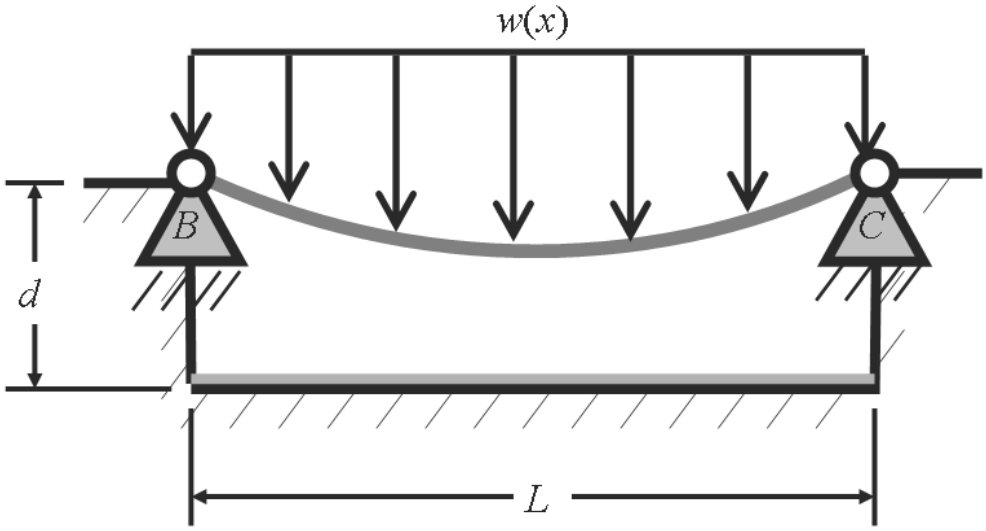

Figure 14. Model of a doubly pinned nanotube.

In this system, Point *B* and *C* are assumed two pinned points, and then there is no slip and vertical motion at *B* and *C*. This assumption is equivalent to neglect the bending resistance at the ends of the nanotube and give an upper bound on the deflection. Thus, the nanotube can be considered as a doubly pinned beam in Section 1. When the voltage difference is applied between the nanotube and the electrode, the deflection in Section 1 can be considered as doubly pinned beam shown in Figure 14. Due to the ends pinned horizontally, the nanotube can not contract along horizontal direction like a simply supported beam when deflecting. Thus, the stretching effect is also considered during deflecting, and then the governing equation is same as Eqn. (50):

$$EI\frac{d^4y}{dx^4} - T\frac{d^2y}{dx^2} = w_e(x) + w_{vdW}(x)$$

where $w_e(x)$ and $w_{vdW}(x)$ are the electrostatic force given by Eqn. (47), and van der Waals force given by Eqn. (48), respectively, and T is the internal tensile force given by Eqn. (61):

$$T = \frac{EA}{2L}\int_0^L \left(\frac{dy}{dx}\right)^2 dx$$

The boundary conditions for both the pinned ends are given by:

$$y(0) = 0, y(L) = 0, y''(0) = 0, y''(L) = 0$$

During the bending process, the nanotube is also applied by the van der Waals force in Section 2. However, for a nanotube with 30nm of Section 2 and 300nm of Section 1, the value of van der Waals force is less than 1% of the electrostatic force. Thus this effect of van der Waals is negligible.

8.2 Nanowire

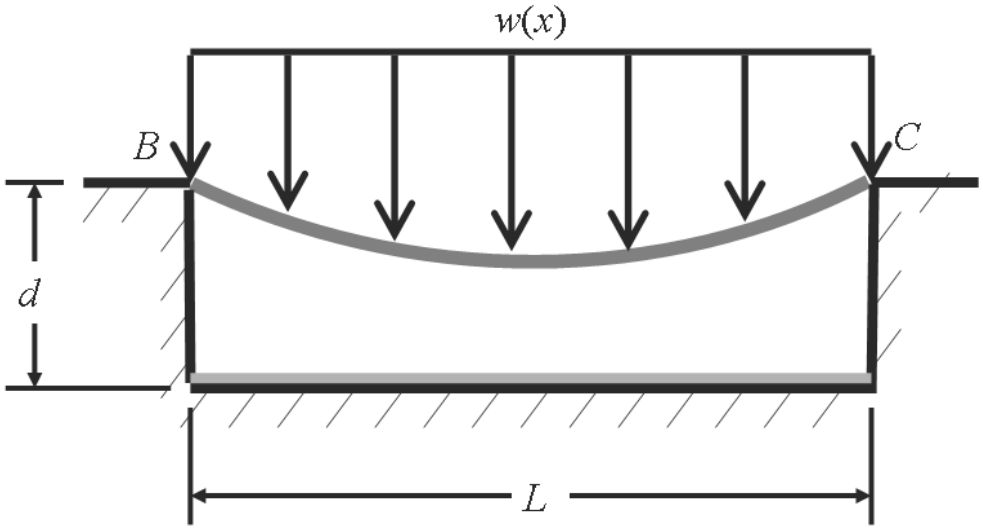

Figure 15. Model of a nanowire.

The structure of the model for a nanowire shown in Fig. 15 is similar as a doubly pinned nanotube, but the bending stiffness *EI* vanishes. Then the governing equation is given by:

$$-T\frac{d^2y}{dx^2} = w_e(x) + w_{vdW}(x) \tag{64}$$

where $w_e(x)$ and $w_{vdW}(x)$ are the electrostatic force given by Eqn. (47), and van der Waals force given by Eqn. (48), respectively, and T is the internal tensile force given by Eqn. (61):

$$T = \frac{EA}{2L}\int_0^L \left(\frac{dy}{dx}\right)^2 dx$$

To assure the model of nanowire does not snap through directly, an external tensile force $T_0 = 2EI/L^2$ is applied on the nanowire initially. Then the internal tensile force becomes:

$$T = \frac{EA}{2L}\int_0^L \left(\frac{dy}{dx}\right)^2 dx + \frac{2EI}{L^2} \tag{65}$$

The boundary conditions for a wire are given by:

$$y(0) = 0, y(L) = 0$$

Chapter 9. Numerical Methods

9.1 Finite difference method

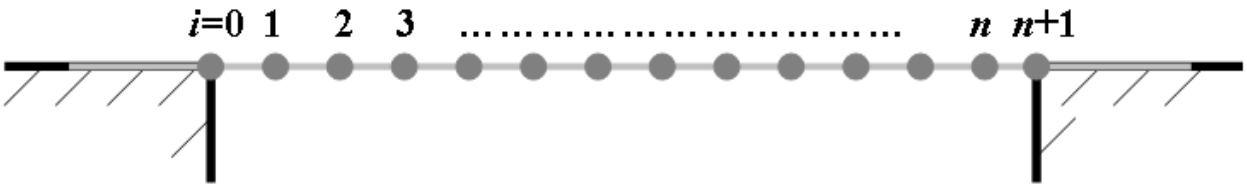

Figure 16. Scheme of a numericalized nanotube.

In the numerical method, the carbon nanotube is divided of n+2 discrete points shown in Fig. 16. The analytic fourth derivative and the second derivative approximate the numerical form [29]:

$$y_i^{(4)} \approx \frac{y_{i-2} - 4y_{i-1} + 6y_i - 4y_{i+1} + y_{i+2}}{\eta^4}$$

$$y_i'' \approx \frac{y_{i-1} - 2y_i + y_{i+1}}{\eta^2}$$

where i is the number for each discrete point, which is from 0 to n+1, y_i presents the value of y at each discrete point, η is the distance between each two points, that is $\eta = L/(n - 1)$. Then the Eqn. (50) approximates:

$$\frac{y_{i-2} - 4y_{i-1} + 6y_i - 4y_{i+1} + y_{i+2}}{\eta^4} - \frac{T}{EI}\frac{y_{i-1} - 2y_i + y_{i+1}}{\eta^2} = w_e(y_i) + w_{vdW}(y_i) \qquad (66)$$

where $w_e(y_i)$ and $w_{vdW}(y_i)$ are the electrostatic force given by Eqn. (47) and van der Waals force given by Eqn. (48) respectively, and T is the internal tensile force. $w_e(y_i)$ and $w_{vdW}(y_i)$ are presented in numerical form of $w_e(x)$ and $w_{vdW}(x)$

In order to substitute the boundary conditions into Eqn. (66), the boundary conditions are applied into the difference form:

$$y(0) = 0 \rightarrow y_0 = 0$$

$$y'(0) = 0 \rightarrow \frac{-y_{-1} + y_1}{2\eta} = 0 \rightarrow y_{-1} = y_1$$

$$y(L) = 0 \rightarrow y_{n+1} = 0$$

$$y'(L) = 0 \rightarrow \frac{-y_n + y_{n+2}}{2\eta} = 0 \rightarrow y_{n+2} = y_n$$

Substitute these boundary conditions into Eqn. (66), it becomes

$$\left(7 + \frac{2T\eta^2}{EI}\right)y_1 - \left(4 + \frac{T\eta^2}{EI}\right)y_2 + y_3 = \left[w_e(y_1) + w_{vdW}(y_1)\right]\eta^4 \quad \text{for} \quad i = 1 \tag{67}$$

$$y_{i-2} - \left(4 + \frac{T\eta^2}{EI}\right)y_{i-1} + \left(6 + \frac{2T\eta^2}{EI}\right)y_i - \left(4 + \frac{T\eta^2}{EI}\right)y_{i+1} + y_{i+2} = \left[w_e(y_i) + w_{vdW}(y_i)\right]\eta^4$$

$$\text{for} \quad i = 2 \ldots n-1 \tag{68}$$

$$y_{n-2} - \left(4 + \frac{T\eta^2}{EI}\right)y_{n-1} + \left(7 + \frac{2T\eta^2}{EI}\right)y_n = \left[w_e(y_n) + w_{vdW}(y_n)\right]\eta^4 \quad \text{for} \quad i = n \tag{69}$$

Combine Eqn. (67), Eqn. (68), and Eqn. (69) into matrix form, that is

$$\begin{bmatrix}
\left(7 + \frac{2T\eta^2}{EI}\right) & -\left(4 + \frac{T\eta^2}{EI}\right) & 1 & & & & \\
-\left(4 + \frac{T\eta^2}{EI}\right) & \left(6 + \frac{2T\eta^2}{EI}\right) & -\left(4 + \frac{T\eta^2}{EI}\right) & 1 & & & \\
1 & -\left(4 + \frac{T\eta^2}{EI}\right) & \left(6 + \frac{2T\eta^2}{EI}\right) & -\left(4 + \frac{T\eta^2}{EI}\right) & 1 & & \\
 & \ddots & \ddots & \ddots & \ddots & & \\
 & 1 & -\left(4 + \frac{T\eta^2}{EI}\right) & \left(6 + \frac{2T\eta^2}{EI}\right) & -\left(4 + \frac{T\eta^2}{EI}\right) & 1 & \\
 & & 1 & -\left(4 + \frac{T\eta^2}{EI}\right) & \left(6 + \frac{2T\eta^2}{EI}\right) & -\left(4 + \frac{T\eta^2}{EI}\right) & \\
 & & & 1 & -\left(4 + \frac{T\eta^2}{EI}\right) & \left(6 + \frac{2T\eta^2}{EI}\right) &
\end{bmatrix}
\begin{bmatrix} y_1 \\ y_2 \\ y_3 \\ \vdots \\ y_{n-2} \\ y_{n-1} \\ y_n \end{bmatrix}
= \eta^4
\begin{bmatrix} w_e(y_1) + w_{vdW}(y_1) \\ w_e(y_2) + w_{vdW}(y_2) \\ w_e(y_3) + w_{vdW}(y_3) \\ \vdots \\ w_e(y_{n-2}) + w_{vdW}(y_{n-2}) \\ w_e(y_{n-1}) + w_{vdW}(y_{n-1}) \\ w_e(y_n) + w_{vdW}(y_n) \end{bmatrix} \tag{70}$$

9.2 Fixed point method

Equation (70) can also be presented simply as

$$A(y)y = b(y) \tag{71}$$

where

$$A(y) = \begin{bmatrix} \left(7+\frac{2T\eta^2}{EI}\right) & -\left(4+\frac{T\eta^2}{EI}\right) & 1 & & & & \\ -\left(4+\frac{T\eta^2}{EI}\right) & \left(6+\frac{2T\eta^2}{EI}\right) & -\left(4+\frac{T\eta^2}{EI}\right) & 1 & & & \\ 1 & -\left(4+\frac{T\eta^2}{EI}\right) & \left(6+\frac{2T\eta^2}{EI}\right) & -\left(4+\frac{T\eta^2}{EI}\right) & 1 & & \\ & \ddots & \ddots & \ddots & \ddots & & \\ & & 1 & -\left(4+\frac{T\eta^2}{EI}\right) & \left(6+\frac{2T\eta^2}{EI}\right) & -\left(4+\frac{T\eta^2}{EI}\right) & 1 \\ & & & 1 & -\left(4+\frac{T\eta^2}{EI}\right) & \left(6+\frac{2T\eta^2}{EI}\right) & -\left(4+\frac{T\eta^2}{EI}\right) \\ & & & & 1 & -\left(4+\frac{T\eta^2}{EI}\right) & \left(6+\frac{2T\eta^2}{EI}\right) \end{bmatrix}$$

$$y = \begin{bmatrix} y_1 \\ y_2 \\ y_3 \\ \vdots \\ y_{n-2} \\ y_{n-1} \\ y_n \end{bmatrix}, \quad b(y) = \eta^4 \begin{bmatrix} w_e(y_1) + w_{vdW}(y_1) \\ w_e(y_2) + w_{vdW}(y_2) \\ w_e(y_3) + w_{vdW}(y_3) \\ \vdots \\ w_e(y_{n-2}) + w_{vdW}(y_{n-2}) \\ w_e(y_{n-1}) + w_{vdW}(y_{n-1}) \\ w_e(y_n) + w_{vdW}(y_n) \end{bmatrix}$$

Multiply $A^{-1}(y)$ in both sides of Eqn. (71), and then

$$y = A^{-1}(y)b(y) \tag{72}$$

The fixed-point method [30, 31] provide a simple way to solve Eqn. (72), that is

$$y^{k+1} = A^{-1}(y^k)b(y^k) \tag{73}$$

where k means the iterative numbers. To solve Eqn. (73), an initial guess y^0 shall be assumed and substituted into the right hand side of Eqn. (73), and then a new set of y^1 will be produced in the

left hand side. Then follow the steps: (1) put the old set of y^k in the right hand side of Eqn. (73), and a new set of y^{k+1} is produced in the left hand side of Eqn. (73), (2) set $y^{k+1} = y^k$, (3) iterate the previous steps. When Eqn. (73) is iterated for infinite times ($k \to \infty$), the approximate solution by iteration will approach the exact solution:

$$\lim_{k\to\infty} y^k = y_{exact}$$

Note that the value of the internal tensile force T is also updated with $A^{-1}(y)$ updated in the right hand side of Eqn. (73). The value of T can be obtained easily by a given set of y_i through calculation of MATLAB.

9.3 Criterion for convergence of numerical solutions

Equation (74) represents the mean difference between old and new solutions during iterating for each voltage:

$$e_i = \frac{\sum_{i=1}^{n} \left| y_i^{k+1} - y_i^k \right|}{n} \le tol \tag{74}$$

where k is the iterative number. The tolerance of error is chosen as $tol = d \times 10^{-4}$ in this study.

Chapter 10. Discussion

In this study, we consider $d = 20nm$, $b = 0.65nm$, and a CNT with $L = 300nm$, $R = R_{ext} = 0.65nm$, $R_{int} = 0$, and $E = 1TPa$. Recall in this study, the effect of van der Waals force is neglected.

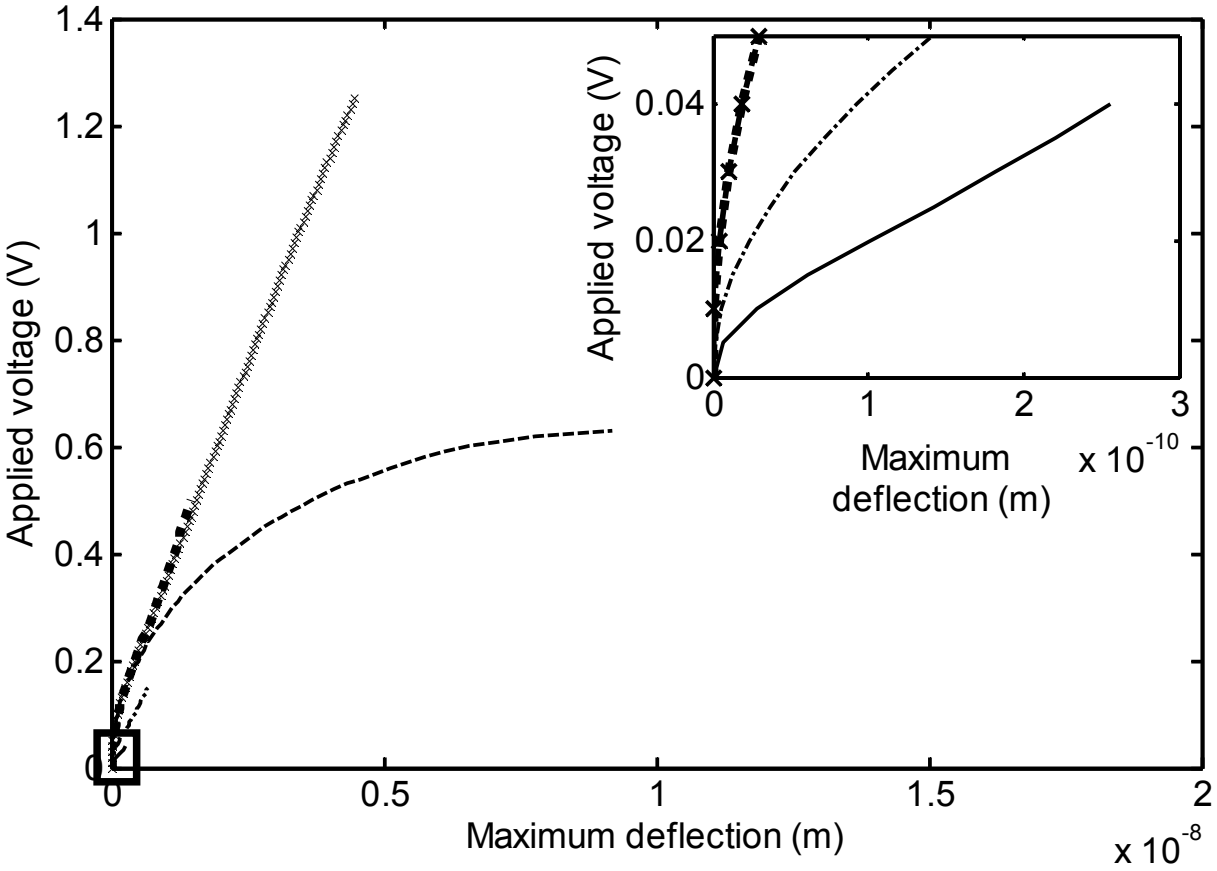

Figure 17. Applied voltages versus maximum deflections. The results are (- -) for a doubly clamped nanotube neglecting stretching effect, (.) for a doubly clamped nanotube with stretching effect but no slip zones, (×) for a doubly clamped nanotube with stretching effect and slip zones ($\tau = 1MPa$), (- . -) for a doubly pinned nanotube with stretching effect, and (-) for a nanowire.

Figure 17 presents the numerical solutions for the maximum deflection y_{max} versus the applied voltage in the equilibrium state, and the right-top figure presents the detail in the left-bottom rectangle. The result represents that a doubly clamped nanotubes needs larger pull-in voltage for the process of snap-through due to its two fixed boundaries. Two interactive moments are produced by both its boundaries in order to resist the bending moments, which the nanotube exerts on both its boundaries. It makes a doubly clamped nanotube which needs larger external load for bending. On the other hand, a doubly pinned nanotube can not afford much external force or voltage because of its free rotational boundaries. It causes a quick snapthrough for a doubly pinned nanotube. The nanotube will afford the smallest voltage if the bending stiffness *EI* is neglected, or a nanotube is stimulated as a wire.

The internal tensile force is a significant role in this analysis. The tensile stresses made by the tensile force also vanishes a portion of bending stresses. Therefore, the deflection for a doubly clamped nanotube with stretching is smaller than one neglecting stretching under the same applied voltage. In other words, a doubly clamped nanotube with stretching looks stiffer than one neglecting stretching. The result in Fig. 18 shows that the effect of the slip zone can reduce a portion of the internal tensile force under the same applied voltage so that the nanotube deflects more easily. However, the internal tensile will be very small and negligible if the deflection of a nanotube is very small compared with its thickness. This also shows in Fig. 17 that the difference of the maximum deflections is not obvious between a doubly clamped nanotube with stretching and one neglecting stretching under a very low applied voltage.

Note that the results are numerical, thus the discussion depends on the convergent numerical solution. In other words, the maximum voltage for each case means “the maximum voltage for solution to converge” rather than “the maximum voltage for snapthrough”. For example, the

solution for a doubly clamped nanotube with stretching effect and slip zones converges under a larger voltage than one with stretching effect but no slip zones. However, the exact maximum voltages for these cases are unknown.

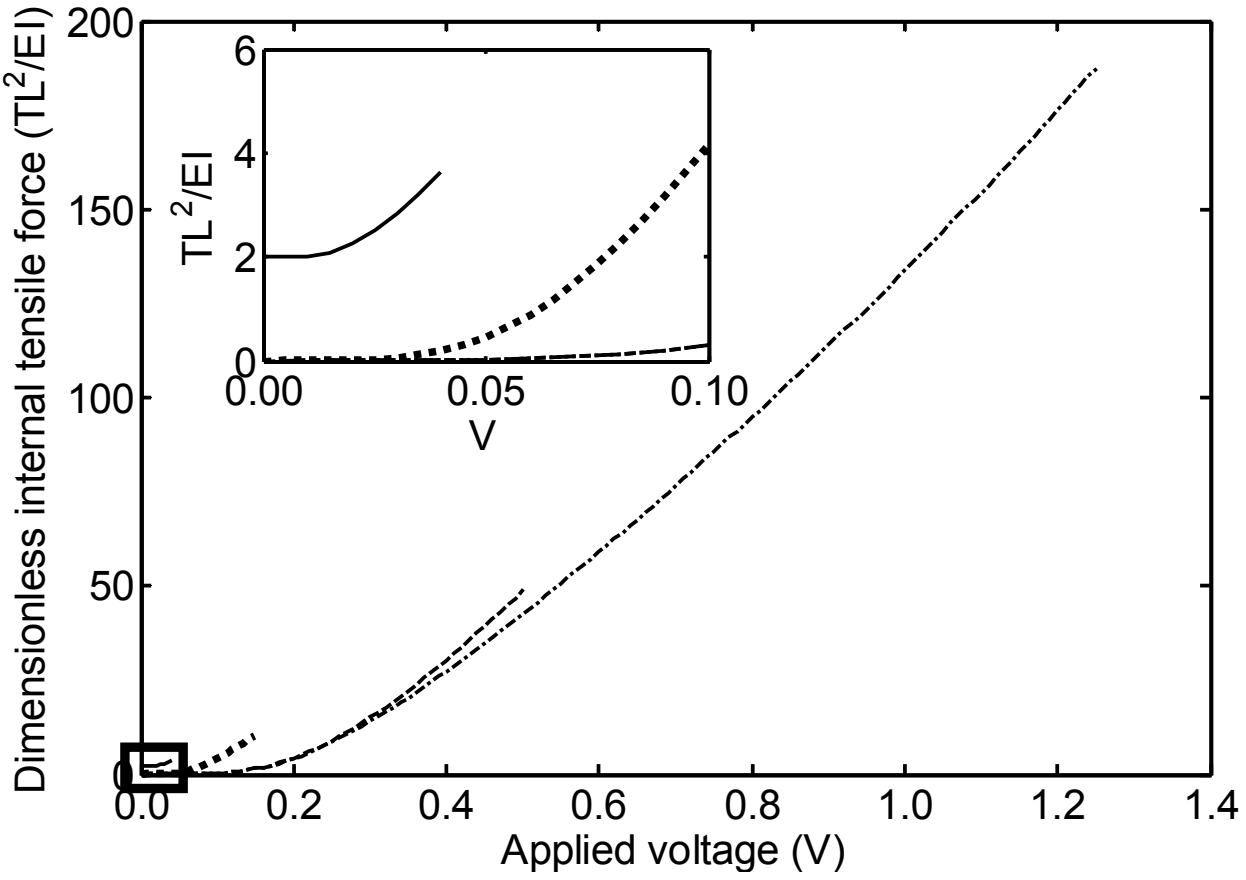

Figure 18. Dimensionless internal tensile forces (TL^2/EI) vs. applied voltages (V). The results are (- -) for a doubly clamped nanotube with stretching effect but no slip zones, (- . -) for a doubly clamped nanotube with stretching effect and slip zones ($\tau = 1MPa$), (.) for a doubly pinned nanotube with stretching effect, and (—) for a nanowire.

Chapter 11. Conclusions

The effect of stretching does not significantly affect the results under a very low voltage or very small deformation. However, the effect of stretching shall be considered when the applied voltage becomes large. For doubly clamped nanotubes with stretching, slip zones can release a portion of the internal tensile force so that a nanotube bends more easily than one without slip zones under the same applied voltage. However, the exactly maximum voltage for snpathrough of each model is still unknown due to the limit of numerical method. Numerically iterative solutions do not converge necessarily (diverge or oscillate) before reaching the maximum voltage for snapthrough. On the other hand, the analytic solution is hard to obtain by solving those governing equations due to the high order nonlinear differential equation. Thus, other methods solving these differential equations will be sought in future investigation.

References

1. Johnson, K. L., *Contact Mechanics*, Cambridge University Press, 1985.
2. Tabor, D., *The Hardness of Metals*, Clarendon Press, 1951.
3. Chang, W. R., Etsion, I., and Bogy, D. B., "Static Friction Coefficient Model for Metallic Rough Surface," *Journal of Tribology*, Vol. 110, pp. 57-63, 1988.
4. Johnson, K. L., Kendall, K., and Roberts, A. D., "Surface Energy and the Contact of Elastic Solids," *Proceedings of the Royal Society of London. Series A, Mathematical and Physical Sciences*, Vol. 324, pp. 301-313, 1971.
5. Derjaguin, B. V., Muller, V. M., and Toporov, Y. P., "Effect of Contact Deformations on the Adhesion of Particles," *Journal of Colloid and Interface Science*, Vol. 53, pp. 314-326, 1975.
6. Tabor, D., "Surface Force and Surface Interactions," *Journal of Colloid and Interface Science*, Vol. 58, pp. 2-13, 1977.
7. Muller, V. M., Yushchenko, V. S., and Derjaguin, B. V., "On the Influence of Molecular Forces on the Deformation of an Elastic Sphere and its Sticking to a Rigid Plane," *Journal of Colloid and Interface Science,* Vol. 77, pp. 91-101, 1980.
8. Greenwood, J. A., "Adhesion of Elastic Spheres," *Proceedings of the Royal Society of London,* Vol. A453, pp. 1277-1297, 1997.
9. Maugis, D., "Adhesion of Spheres: The JKR-DMT Transition Using a Dugdale Model," *Journal of Colloid and Interface Science*, Vol. 150, pp. 243-269, 1992.
10. Greenwood, J. A., and Johnson, K. L., "An Alternative to the Maugis Model of Adhesion between Elastic Spheres", *Journal of Physics D: Applied Physics*, Vol. 31, pp. 3279-3290, 1998.

11. Barthel, E., "On the Description of the Adhesive Contact of Spheres with Arbitrary Interaction Potentials," *Journal of Colloid and Interface Science*, Vol. 200, pp. 7-18, 1998.
12. Kadin, Y., Kligerman, Y., and Etsion, I., "Jump-In Induced Plastic Yield Onset of Approaching Microcontacts in the Presence of Adhesion," *Journal of Applied Physics,* Vol. 103, pp. 013513-1–013513-8, 2008.
13. Maugis, D., *Contact, Adhesion and Rupture of Elastic Solids*, Springer Co., 2000.
14. Qian, D., Wagner, G. J., Liu, W. K., Yu., M., and Ruoff, R. S., *Mechanics of Carbon Nanotubes*, Appl Mech Rev, **55**, 2002, pp. 495-533.
15. Kim, P., and Lieber, C. M., *Nanotube Nanotweezers*, Science, **286**, 1999, pp. 2148-2150.
16. Rueckes, T., Kim, K., Joselevich, E., Tseng, G. Y., Cheung, C., and Lieber, C. M., *Carbon Nanotube-Based Nonvolatible Random Access Memory for Molecular Computing*, Science, **289**, 2000, pp. 94-97.
17. Kinaret, J. M., Nord, T., and Viefers, S., *A Carbon-Nanotube-Based Nanorelay*, Applied Physics Letters, **82**, 2003, pp. 1287-1289.
18. Fennimore, A. M., Yuzvinsky, T. D., Han, W., Fuhrer, M. S., Cumings, J., and Zettl, A., *Rotational Actuators Based on Carbon Nanotubes*, Nature, **424**, 2003, pp. 408-410.
19. Dequesnes, M., Rotkin, S. V., Aluru N. R., *Calculation of Pull-in Voltages for Carbon-Nanotube-Based Nanoelectromechanical Switches*, Nanotechnology, **13**, 2002, pp. 120-131.
20. Simitses, G. J., An Introduction to the Elastic Stability of Structures, Robert E. Krieger Publishing Company, Inc., 1986.
21. Akita, S., Nakayama, Y., Mizooka, S., Takano, Y., Okawa, T, Miyatake, Y., Yamanaka, S., Tsuji, M., Nosaka, T., *Nanotweezers consisting of carbon nanotubes operating in an atomic*

force microscope, Applied Physics Letter, **79**, pp. 1681-1693.

22. Dequesnes, M., Tang, Z., Aluru N. R., *Static and Dynamic Analysis of Carbon Nanotube-Based Switches*, Journal of Engineering Materials and Technology, **126**, 2004, pp. 230-237.
23. Ke, C., Espinosa, H. D., and Pugno, N., *Numerical Analysis of Nanotube Based NEMS Devices — Part II: Role of Finite Kinematics, Stretching and Charge Concentrations*, Journal of Applied Mechanics, **72**, 2005, pp. 726-731.
24. Ke, C., and Espinosa, H. D., *Numerical Analysis of Nanotube Based NEMS Devices — Part I: Electrostatic Charge Distribution on Multiwalled Nanotubes*, Journal of Applied Mechanics, **72**, 2005, pp. 721-725.
25. Cheng, D., *Field and Wave Electromagnetics*, Addison-Wesley Publishing Company, Inc., 1989, pp. 133-143.
26. Girifalco, L. A., Hodak, M, amd Lee, R. S., *Carbon Nanotubes, Buckyballs, Ropes, and a Universal Graphitic Potential*, Physical Review B, **62**, 2000, pp. 13104-13110.
27. Hibbeler, R. C., Mechanics of Materials, 4th Ed., Prentice-Hall International, Inc., 2000, pp. 264-265.
28. Budynas, R. G., *Advanced Strength and Applied Stress Analysis*, 2nd Ed., McGraw-Hill, pp. 471-482.
29. Fausett, L. V., Applied Numerical Analysis Using MATLAB, 2nd Ed., Pearson Prentice Hall, 2008, pp. 576-581.
30. Quarteroni, A., Sacco, R., Saleri, F., Numerical Mathematics, 2nd Ed., Springer Co., 2007, pp. 295-299.
31. Walter, G., Numerical Analysis: an introduction, Birkhauser Boston, 1997, pp. 241-242.